3366 Vol. 65, No. 10 / 1 April 2026 / Applied Optics Research Article

applied optics

Fabry–Perot cascade interferometer for temperature measurement of Si microstructures

Didier Beghuin,[1,*] John Bigeon,[1] Maria Lopera-Acosta,[2] Hans Samsom,[3] Frederic Duflos,[4] Wout Peeters,[5] and Alexis Humblet[3]

[1] Lambda-X High Tech SRL, Rue Robert Schuman 102, 1400 Nivelles, Belgium
[2] Vrije Universiteit Brussel, Pleinlaan 2, 1050 Brussels, Belgium
[3] IMEC, Kapeldreef 75, 3001 Leuven, Belgium
[4] Duflos Comm.V, 3210 Lubbeek, Belgium
[5] TMC Europe, Da Vincilaan 11, 1935 Zaventem, Belgium
*dbeghuin@lambda-x.com

Received 2 February 2026; revised 6 March 2026; accepted 11 March 2026; posted 11 March 2026; published 27 March 2026

Silicon MEMS micromirrors face critical thermal challenges from high optical loads, requiring accurate temperature validation for reliable design. Finite element thermal models are hindered by parameter uncertainties, while standard non-contact measurement methods fail for thin silicon structures. We present a novel optical technique, to our knowledge, using coherence-tuned Fabry–Perot interferometry to accurately measure the micromirror plate temperature. By employing two sequential interferometers with an incoherent source, we selectively isolate the temperature-dependent refractive index change in the mirror plate, excluding parasitic reflections from the underlying substrate. The method achieves temperature uncertainty on the order of ±2°C across the 40°C–200°C range when calibrated against a thermistor. This approach enables thermal characterization of MEMS devices where conventional contact-based methods are impractical.

https://doi.org/10.1364/AO.590792

1. INTRODUCTION

Silicon micro-electro-mechanical systems (MEMS) micromirrors are widely used in applications where they are exposed to significant thermal loads. For instance, in laser beam and pulse shaping or free-space optical communication systems, high optical power can lead to substantial heat generation within the MEMS structure [1,2]. Similarly, in advanced lithography processes, such as deep ultraviolet (DUV) and extreme ultraviolet (EUV) [3,4], limitations in reflective coating performance, combined with increasing source power and operation at low pressure, result in a considerable temperature rise in the MEMS structure.

Elevated micromirror temperatures can cause several detrimental effects. For example, temperatures above 250°C can damage gold reflective coatings [5], while even lower temperatures can significantly impact performance through mirror surface deformation, reduced actuation force of piezoelectric actuators, performance degradation of reflective coatings, and an overall increase in failure rates. These challenges impose strict design trade-offs, as achieving a large displacement range requires low-stiffness structures, while ensuring thermal robustness demands high-thermal-conductivity elements. These objectives often conflict since thin, compliant suspension beams inherently limit heat conduction to the substrate.

Thermal behavior is typically predicted through finite element method (FEM) simulations during the design phase. However, these models often involve hundreds of parameters for complex designs, many of which are uncertain or unavailable. For example, thin-film thermal conductivity may differ from bulk values and is rarely documented in material databases; nonlinear temperature-dependent material properties are often neglected; and constitutive properties of thin-film materials can vary significantly depending on the precise process sequence [6]. Moreover, discrepancies between the as-built geometry and the modeled structure can further increase the uncertainty. Consequently, experimental validation of thermal simulations is essential to ensure accurate performance predictions.

Accurate experimental validation requires measuring the mirror plate temperature under realistic operating conditions. The mirror plate itself is a silicon structure, typically 40–80 μm thick, suspended on thin hinges over a complex substrate. In a vacuum environment, commonly required to maximize the quality factor or to prevent beam distortion and gas breakdown, the main thermal path for heat dissipated on the mirror plate is restricted to conduction toward a heat sink located at the backside of the substrate, making the mirror plate temperature significantly higher than that of the substrate.

Suitable experimental methods are limited in availability. A non-contact technique is essential as any sensor in direct contact with the mirror plate would create a parasitic thermal path. Infrared thermography [7] is not suitable because the mirror plate is a thin silicon structure that is semi-transparent in the mid-wave infrared (MWIR) and long-wave infrared (LWIR) ranges, and applying a high-emissivity coating on the micromirror surface is not an option, as this would compromise any further use of the mirror. Similarly, non-contact ultrasonic methods [8] are impractical due to their complexity and lack of robustness for complex MEMS structures. In [9], a micromirror temperature measurement method based on the change of electrical resistance due to heating is proposed. However, this method requires a dedicated test structure with embedded resistive elements rather than measurements on functional devices, limiting its applicability for complex devices where embedding a temperature sensor on the mirror plate is not possible. Raman spectroscopy [10], though highly accurate, presents significant integration challenges. Consequently, we evaluated the measurement of the temperature-dependent refractive index as a practical alternative. This approach offers high sensitivity for wavelengths near the silicon bandgap and can be implemented through a reasonably straightforward optical setup.

This thermo-optic effect is particularly pronounced in semiconductors for electromagnetic radiation energies approaching the bandgap energy. This phenomenon has been previously exploited to realize all-silicon temperature microsensors [11]. Several papers report on the thermo-optic coefficient of silicon in the short-wave infrared (SWIR) region. A value of $dn/dT = 1.85 \times 10^{-4}\ \mathrm{K}^{-1}$ for crystalline silicon at 300 K for a wavelength of 1523 nm has been reported [12,13], with nonlinear temperature dependence. For shorter wavelengths, closer to the silicon bandgap, one can expect the thermo-optic coefficient to be larger than at 1523 nm. Experimental data for silicon refractive index variations across wavelengths from 1.1 to 5.7 μm and temperatures from 50 to 295 K are available [14]. At 1.1 μm, the refractive index values of 3.56 at 295 K [14] and 3.54 at 300 K [15] have been measured; we adopt the value of 3.54 for numerical simulations in this work.

2. METHOD

The structure of interest, the micromirror plate, a silicon parallel window of typically 70 μm thickness, can be considered as a Fabry–Perot (FP) cavity. The coefficients of reflection of each interface are governed by the Fresnel law of reflection (Si-vacuum interface). As the temperature increases, the silicon refractive index increases and thereby the cavity optical path length (OPL). Thus, by monitoring the evolution of the reflected interference generated by this FP cavity, the silicon temperature can be accurately estimated. For monochromatic incident light, temperature modulates the reflected beam intensity by changing the cavity OPL. The reflection pattern is periodic, with its phase linked to temperature; therefore, the method is based on phase retrieval from the interference signal.

The FP cavity sits on top of a complex underlying structure, making the transmitted beam impossible to access directly. Additionally, multiple reflections from underlying layers generate complex interference patterns in the reflection path that become difficult to interpret when the temperature changes. As the setup aims to determine the temperature of the top plate only, we tune the light coherence to solely probe this element while excluding contributions from the substrate. This ensures that only the top window contributes to the measured interference pattern.

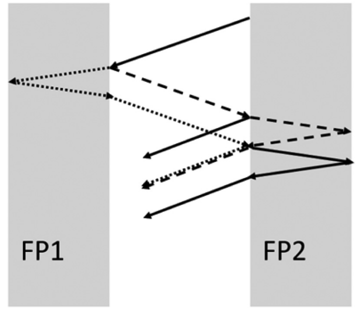

Fig. 1. Conceptual schematic of the cascaded configuration: the primary FP cavity (FP1) serves to selectively probe the optical properties of the micromirror plate (FP2).

The selected solution is to start with a low temporal and spatial coherence LED and to prepare its temporal coherence with a first FP cavity (FP1 in Fig. 1) before the light is projected on the second cavity (FP2 in Fig. 1), i.e., the Si mirror plate whose temperature varies. Figure 1 also shows how some of the ray combinations interfere as the ray paths represented by the dashed lines (short and long) have the same optical path length. The temporal coherence preparation by the first cavity ensures that one sees fringe contrast for optical cavity lengths that are very similar in the two FP interferometers. Indeed, if the optical cavity length difference between the two FP is larger than the original temporal coherence of the source, the visibility of the fringes will disappear.

To ensure that the interference in the second FP leads to fringe visibility, one images the first FP to the second one with simple achromatic lenses. By doing this, we ensure that spatial coherence is also controlled. The spatial coherence of the original source can also be experimentally tuned by a variable aperture properly set in an intermediate image plane of the LED-emitting chip.

3. OPTICAL SETUP

The schematic of the optical setup is represented in Fig. 2. A 1050 nm central wavelength LED light source (Thorlabs LED1050L2) is imaged in a variable aperture used to control its spatial coherence and intensity, thanks to a short focal length lens L1.

L2 and L3 are 100 mm focal length lenses (Thorlabs AC254-100) placed such that the reference FP cavity (Ref FP) is projected on the sample FP cavity with a magnification of 1. For the reference FP cavity, we typically use a MEMS mirror from the same fabrication batch. L4 is a 150 mm focal length achromat (Thorlabs AC254-150) imaging the sample FP onto the camera (Baumer VCXG2.32M) with 1.5 magnification.

A first polarizing beam splitter (PBS, Thorlabs ccm1_pbs255) directs the LED radiation toward the reference FP cavity. Radiation reaches it after passing through L2 and

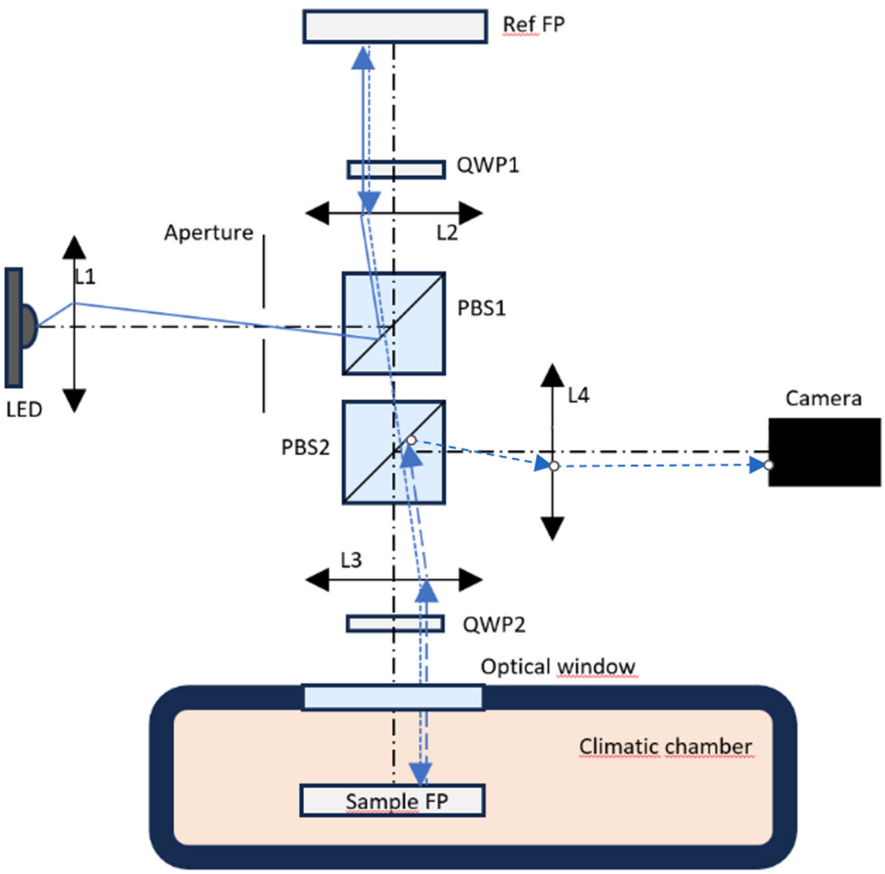

Fig. 2. Schematic of the optical setup. PBS, polarizing beam splitter; FP, Fabry–Perot; L, lens; and QWP, quarter-waveplate.

a first quarter-waveplate (QWP). After interfering in the first FP (reference FP) cavity, the reflected radiation polarization is rotated from the original s-state to the p-state via a double pass through the QWP. When entering the first PBS in the reflection path, the radiation is fully transmitted.

The same combination of PBS, lens, and QWP is used for the lower part of the setup, towards the sample FP cavity, leading finally to an efficient transmission of the radiation toward the camera.

The imaging configuration facilitates the retrieval of spatial information, enabling the precise identification of regions of interest. With real-time imaging, we ensure that the reference FP is imaged on the sample FP by adequate lateral positioning. Due to slight imperfections in the parallelism and uniformity of the FP windows, the captured images reveal spatial interference fringes that map the local thickness variations of the silicon structures.

4. SIMULATION OF THE EXPERIMENT

The combined effect of two FP interferometers is modeled using GNU Octave. This numerical study incorporates several simplifying assumptions to model the physical processes:

- The silicon refractive index is supposed to vary linearly with temperature. A value of $dn/dT = 2.07 \times 10^{-4}\ \mathrm{K}^{-1}$ is used, which is close to our experimental values. The 20°C refractive index is taken as 3.54.

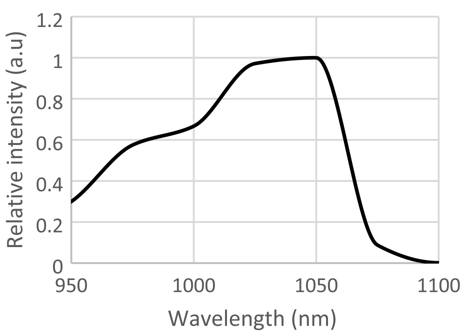

Fig. 3. Spectral power density considered for the simulation, being the multiplication of the LED source spectral density by the camera spectral response.

- The simulation is scalar; no polarization-related effects are considered; in other terms, we assume that the Si birefringence is negligible.
- An approximation of the spectral content of the radiation combined with the spectral response of the camera corresponding to Fig. 3, is used.
- The spectral absorption of silicon at 300 K is retrieved from [16].
- The variation of silicon absorption with temperature is not considered.
- The nominal thicknesses of the two FP cavities are defined as 70 and 71 µm, respectively.

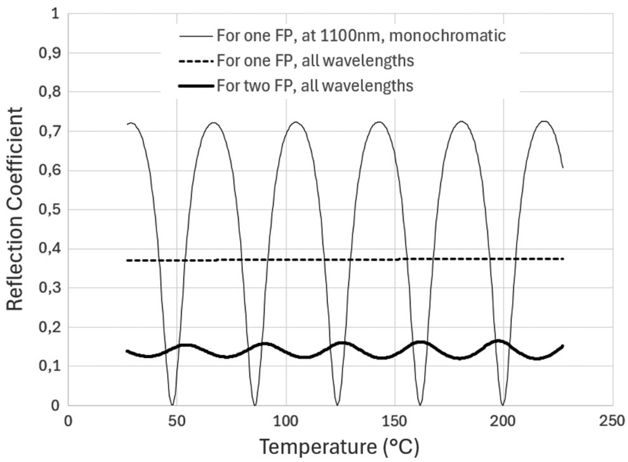

Fig. 4. Reflection coefficients for different simulation conditions; thin solid curve: a single silicon FP cavity is simulated with a single wavelength (here 1100 nm), and the temperature of this cavity is varying; dashed curve: a single FP cavity with all wavelengths, the temperature of the cavity is varying; thick curve: reflection on two FP cavities; the first one is at constant temperature, and the second one has its temperature varying.

- The simulation is run only at one single point, assuming parallel beams, without considering any spatial coherence-related effects.

The simulation results are shown in Fig. 4 for several conditions. The first simulation assumes monochromatic incident light on a single FP cavity whose temperature varies from 27°C to 227°C. The result is shown as the thin solid curve in Fig. 4 and can be obtained from the classical Fabry–Perot equation (see, e.g., [17]).

When the spectrum of Fig. 3 is considered with a single FP cavity, we obtain the dashed curve shown in Fig. 4. Here, the output intensity remains nearly constant with the temperature due to the limited temporal coherence of the source. Since the optical cavity length exceeds the source coherence length, the reflected waves from different wavelengths contribute to a wide range of phases. These incoherent contributions sum to eliminate any interference contrast in the reflection.

The results using two FP cavities, such as in our experimental setup, are shown as a thick curve in Fig. 4. In this case, light is reflected by the first FP at constant temperature and again reflected by the second FP cavity with varying temperature. The interference pattern contrast is at its best 18%, and it varies with temperature. This contrast change is due to the optical cavity length of the second FP cavity increasing with the temperature. If the OPL difference between the two cavities exceeds the temporal coherence length of the source, the fringe contrast disappears. The reflected interference signal from the second cavity is approximately sinusoidal, which facilitates phase retrieval.

5. IMAGE PROCESSING METHODOLOGY

The optical imaging system projects both FP cavities onto the camera sensor, with the first cavity imaged onto the second and both subsequently imaged onto the camera. Optical path difference variations across the micromirror produce spatial fringes on the camera image. We exploit spatial information to facilitate the retrieval of the interference pattern phase shift.

To estimate the evolution of the fringe phase with temperature, we model the mean-removed 2D fringe signal observed in each image as

$$s[m, n] = A\cos(2\pi(f_n n + f_m m) + \varphi) + w[m, n],$$

where A is the fringe amplitude, m and n are pixel indices, f_n and f_m are the spatial frequencies along the two image axes, φ is the fringe phase, and $w[m, n]$ is zero-mean white Gaussian noise. Sinusoidal parameters are estimated using the approximate maximum likelihood approach described in [18]. First, the spatial frequencies are estimated by maximizing the 2D periodogram of the fringe image. Then, with frequencies fixed, the resulting linear maximum likelihood amplitude and phase estimation problem is solved. Frequency estimation is performed only once per image set. In practice, the region of interest (ROI) must be limited to ensure that the sinusoidal model remains accurate. Regions of approximately 100–200 µm of lateral dimensions yield reliable phase estimates. Additionally, the ROI is selected to avoid clutter caused by substrate structures visible through the mirror plate, which could distort the fringe pattern.

6. EXPERIMENTAL RESULTS

A. Comparison to a Reference Sensor

To validate the proposed method, we place a micromirror array (MMA) die on a thermoelectric cooler (TEC—Laird ETX2-12-F2-3030-TA-W6) in a low-pressure (3.8 Pa) nitrogen environment [Fig. 5(a)]. A negative temperature coefficient (NTC) thermistor (TDK B57540G1) is attached to the die using thermally conductive adhesive [EPOTEK H21D, Fig. 5(b)]. No heat-generating optical load is applied during this phase (the load from the 1050 nm LED used for imaging is considered negligible). The NTC provides feedback to a proportional-integral controller (SRS PTC10) that regulates the TEC current, ensuring precise temperature control from room temperature up to 200°C. Backside heating and limited convective and radiative heat transfer ensure a uniform temperature distribution across the micromirror structure.

For the FP reference cavity, we use either another micromirror plate or a thinned silicon wafer fragment; the latter minimizes parasitic optical interference from the underlying MEMS structures. The setup is adjusted to maximize contrast in the interference pattern [Fig. 5(c)].

We record the interference pattern while increasing the die temperature at a controlled rate (~0.5°C/s) to avoid dynamic thermal effects and ensure reliable phase unwrapping at the available camera acquisition rate (2 frames/s). The temperature increase is stopped for a few seconds every minute. The measurements are repeated across multiple samples, regions of interest (ROIs), and maximum temperatures (120°C, 125°C, and 200°C). For each measurement, a small ROI with high-contrast fringes is selected [Fig. 5(d)], and the phase is estimated using the method described in Section 5.

As an example of the different experiments performed, for one specific ROI, the unwrapped phase time evolution is shown

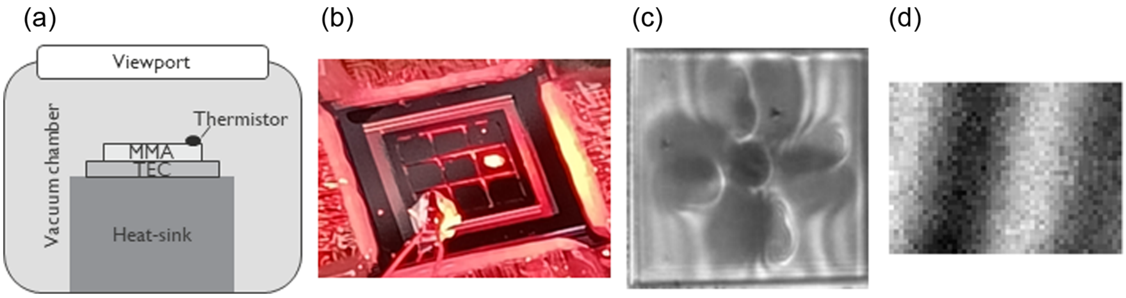

Fig. 5. Temperature measurement: (a) schematic view of the temperature control setup; (b) photograph of the 3 × 3 MMA with a thermistor attached to its lower-left corner; the middle-left mirror is illuminated with a red laser simulating an optical load; each mirror is 1 × 1 mm^2; (c) a pair of micromirrors (reference and sample under test) imaged with the setup of Fig. 2, showing the interference pattern; and (d) typical ROI selected for interference pattern analysis.

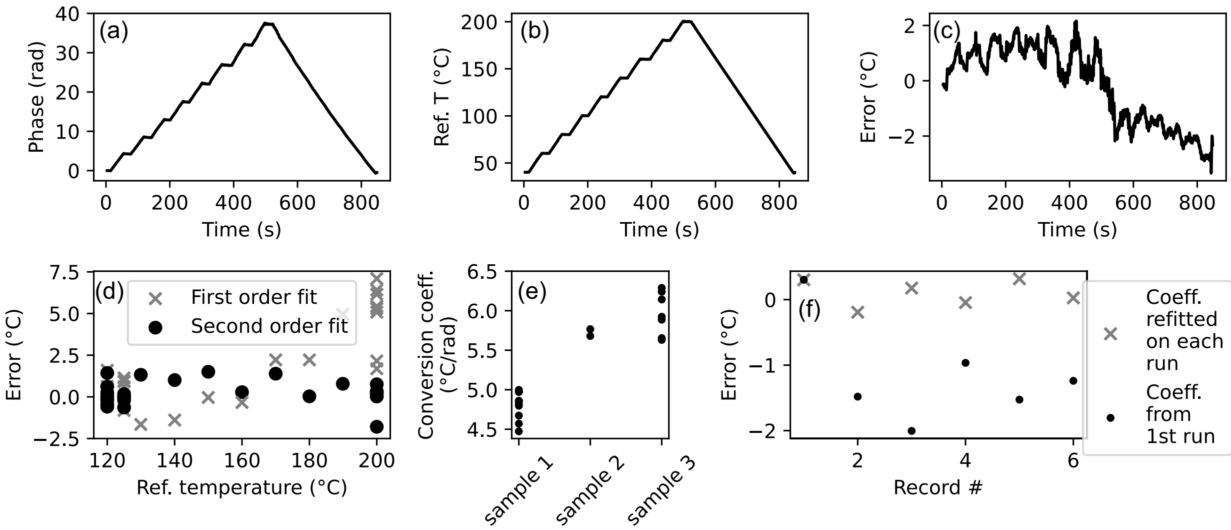

Fig. 6. Method validation results: (a) unwrapped fringe phase estimate for a single validation measurement; (b) NTC measured die reference temperature during the same measurement; (c) difference (residuals) between the temperature estimate (with a second-order-fit) and reference values; (d) temperature residual error at maximum temperature for 22 validation measurements using a linear or second-order fit; (e) linear conversion coefficient for 22 validation measurements on three different samples; and (f) temperature residual error at maximum recorded temperature for six consecutive measurements using the same sample and same ROI.

in Fig. 6(a). The corresponding unwrapped phase is well correlated to the reference temperature, whose time evolution is shown in Fig. 6(b). The reference temperature is fitted to the recovered phase using either a first- or second-order polynomial to obtain a temperature estimation function. The initial temperature (40°C) is assumed to be known. The method measures relative temperature changes only. The temperature error is computed as the difference between the estimated and the reference values, in this case for the second-order polynomial fit [Fig. 6(c)].

Across 22 measurements, a linear fit maintains the error below ±2°C up to 125°C. Above this temperature, the linear fit systematically overestimates the temperature by up to 7.5°C at 200°C. A second-order polynomial fit is required to maintain ±2°C accuracy across the full range [Fig. 6(d)]. A significant variation in the linear coefficient is observed across ROIs and samples [Fig. 6(e)].

To assess the measurement error in an operational calibrate-once-then-measure scenario (Section 6.B), we evaluate the error obtained when reusing coefficients fitted on an initial run. In addition to noise and model-induced terms, this reuse includes a between-runs repeatability component, yielding a typical residual of less than 2°C at the maximum recorded temperature [Fig. 6(f)], whereas refitting on each run gives close to zero residuals. This result holds when calibration and measurement are performed on the same sample and the same ROI.

B. Measurement with an Optical Load

To quantify the temperature increase of a micromirror under an optical load, we proceed in two steps: calibration and measurement.

The calibration step uses the method described in Section 6.A to obtain the polynomial coefficients that convert the fringe phase variations to temperature differences. Calibration is performed over the full temperature range of interest, with the MMA temperature being set by the TEC-controlled temperature and effectively measured with an NTC [Fig. 6(b)]. Although the NTC is attached to a micromirror plate in this experiment, any sensor in contact with the die would

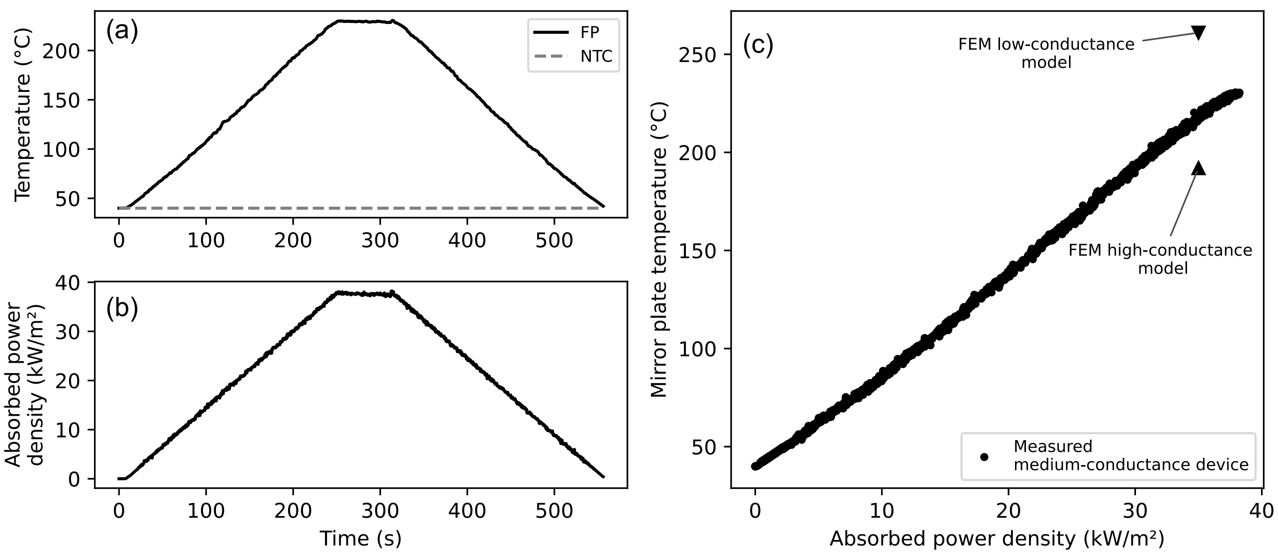

Fig. 7. Temperature measurement under optical load: (a) evolution of the mirror plate and reference NTC temperature. As the optical load is focused on a single mirror, the NTC temperature is not impacted. (b) Absorbed power density during the same measurement. (c) Mirror plate temperature versus absorbed power density with comparison to FEM bounds for two different models (see details in the text).

be sufficient here as its temperature is homogeneous during calibration.

The measurement step starts by stabilizing the device to the initial temperature (40°C) using the TEC and reference NTC sensor. A multimode fiber-coupled high-power 638 nm laser diode is uniformly projected on the micromirror under test to provide the optical loading of up to 80 kW/m^2. The optical power absorbed by the device is estimated to be 60%, considering the transmission through the vacuum viewport and the mirror reflectivity. The optical load is progressively increased. Figure 7(a) shows the estimated temperature (computed from the interference signal phase) evolution for the micromirror irradiated by the optical load, as well as the reference NTC temperature, attached to a micromirror, which is not irradiated. The corresponding optical load is shown in Fig. 7(b). Combining the optical load and the estimated temperature time evolution, we obtain the mirror plate temperature versus the absorbed optical load power density [Fig. 7(c)].

To assess the measurement repeatability, the two-step procedure is repeated five times on the same micromirror. Different but partially overlapping ROIs are selected for each repetition. The mean mirror plate temperature measured at 35 kW/m^2 absorbed optical power density is 217°C, with a sample standard deviation of 1.3°C. The repeatability error includes the contribution from both the interferometric temperature measurement and the applied power density.

At an absorbed optical power density of 35 kW/m^2, the measured mirror-plate temperature of 217°C lies between two uncalibrated FEM variants that enclose the geometry of the fabricated device through slight perturbations of the geometry: the low-conductance variant predicts 261°C, whereas the high-conductance variant predicts 192°C [Fig. 6(f)]. The experimental value, therefore, serves as the reference for potential FEM model calibration. As a next step, the FEM model could be adjusted within known fabrication tolerances to match the measurement, yielding an effective geometric/thermal parameter set; such a calibrated model would enable accurate thermal-performance prediction for subsequent design iterations.

7. DISCUSSION

The absolute temperature uncertainty for a calibrated ROI is on the order of ±2°C. Since a typical 2π phase shift corresponds to 34.5°C, this translates to a phase uncertainty of approximately one period over 20 ($\lambda/20$). We can further estimate the signal-to-noise ratio (SNR) to verify if we are noise-limited or if we are limited by systematic errors. Signal amplitude is calculated using the model and approximate maximum likelihood approach described in Section 5, while intensity noise variance is derived from the variance of the residuals between the measured intensity and the fitted sinusoidal model. The SNR decreases with increasing temperature due to a reduced interference contrast. SNR values for the measurement shown in Fig. 6(a) range from 2.5 at 40°C to 0.5 at 200°C. Given the high number of pixels per ROI (typically more than 2000), the phase estimator variance should theoretically approach the Cramér–Rao lower bound (CRLB) [18]. However, we note that the actual variance is typically 10 to 100 times higher than the CRLB (see Supplement 1), indicating that our measurement is not noise-limited but rather limited by systematic errors and model mismatch. We attribute the reduction of the SNR at high temperature to an increasing optical length mismatch between the two optical cavities. Note that the temperature of the reference mirror was controlled by the room temperature only, thereby bringing some additional uncertainty to the reference FP cavity length. Assuming a micromirror thickness of 70 µm and using the average slope of 5.5°C/rad, we obtain a thermo-optical coefficient of $dn/dT = 2.07 \times 10^{-4}$ K^{-1}, which is consistent with the value of 1.84×10^{-4} K^{-1} previously reported at 1.53 µm wavelength [12]. The temperature-dependent OPL change of the cavity is largely dominated by the refractive index variation in silicon; from the relative magnitudes of the temperature sensitivity of length and refractive index, thermal expansion effects are negligible.

The calibration establishes a reproducible phase-to-temperature relationship for a specific ROI on a given micromirror, but we observe significant variations throughout devices. Within one micromirror, local spatial variations of the phase-to-temperature relationship are also observed. We attribute these mainly to local thickness variations, although this was not experimentally confirmed. Accurate knowledge of the two cavities' thicknesses is required for accurate determination of the thermo-optical coefficients. Using a thickness-calibrated reference silicon cavity would enable absolute thickness determination of the second cavity, but we did not conduct this experiment within the scope of this work.

The data reported in Fig. 7(c) serve as validation and calibration data for FEM simulations of the thermal behavior of the micromirror under optical load. Although a precise description of the thermal model goes beyond the objectives of this paper, we can report that the experimental results validate the main features included in the model, i.e., confirming the negligible contributions of convection and radiation and the high thermal conductance of the micromirror actuation stage.

8. CONCLUSION

We have demonstrated a non-contact temperature measurement for MEMS silicon micromirror plates based on a cascade of two FP interferometers. The method achieves temperature uncertainty on the order of $\pm 2^\circ$C in the 40°C to 200°C temperature range and enables thermal characterization under optical load conditions.

The combination of two FP interferometers, one kept at a constant temperature while the second one has its temperature changing, allows us to link the temperature to the interference phase. The use of an incoherent light source allows us to be sensitive to the OPL of the micromirror plate, only, ensuring that the interference signal is not perturbed by the underlying structures.

Our measurements yield a thermo-optical coefficient for silicon of 2.07×10^{-4} K^{-1} at 1050 nm, consistent with the literature values. Importantly, we find that measurement uncertainty is limited by systematic errors and modeling mismatch rather than detector noise. Spatial variations in the phase-temperature relationship necessitate individual ROI calibration, primarily attributed to local thickness variations.

This approach provides a valuable measurement tool for characterizing thermal behavior in MEMS devices where conventional contact-based methods are impractical, enabling the validation and calibration of thermal models during device development.

Disclosures. Lamdba-X High Tech SRL.

Data availability. Data underlying the results presented in this paper are not publicly available at this time but may be obtained from the authors upon reasonable request. Data related to the micromirror device under testing will not be shared.

Supplemental document. See Supplement 1 for supporting content.

REFERENCES

1. Ç. Ataman, S. Lani, W. Noell, *et al.*, "Fabrication and characterization of 3D integrated 2 DOF Micromirror Arrays for excessive thermal loads," Proc. IEEE MEMS **2011**, 684–687 (2011).
2. P. Do Vale Pereira, M. T. Hunwardsen, and K. Cahoy, "Characterization of laser thermal loading on microelectromechanical systems-based fast steering mirror in vacuum," Opt. Eng. **59**, 056109 (2020).
3. W. Endendijk, M. Mulder, and B. van Drieënhuizen, "Successful implementation of a MEMS micromirror array in a lithography illumination system," Proc. IEEE Transducers **2013**, 2564–2567 (2013).
4. T. Sandner, J. U. Schmidt, H. Schenk, *et al.*, "Highly reflective coatings for micromechanical mirror arrays operating in the DUV and VUV spectral range," Proc. SPIE **5721**, 72–81 (2005).
5. J. Zhang, Y.-C. Lee, A. Tuantranont, *et al.*, "Thermal analysis of micromirrors for high-energy applications," IEEE Trans. Adv. Packag. **26**, 310–317 (2003).
6. S. D. Senturia, "CAD challenges for microsensors, microactuators, and microsystems," Proc. IEEE **86**, 1611–1626 (1998).
7. R. Usamentiaga, P. Venegas, J. Guerediaga, *et al.*, "Infrared thermography for temperature measurement and non-destructive testing," Sensors **14**, 12305–12348 (2014).
8. I. Ihara, M. Takahashi, and H. Yamada, "A non-contact temperature sensing with ultrasound and the potential for monitoring heated materials," Proc. IEEE Sensors **2009**, 1709–1714 (2009).
9. I. Wullinger, D. Rudloff, K. Lukat, *et al.*, "Temperature measurement on MOEMS micromirror plates under illumination," Proc. SPIE **7592**, 75920P (2010).
10. M. R. Abel, T. L. Wright, E. O. Sunden, *et al.*, "Thermal metrology of silicon microstructures using Raman spectroscopy," Proc. IEEE Semi-Therm **2005**, 235–242 (2005).
11. G. Cocorullo, F. G. Della Corte, M. Iodice, *et al.*, "A temperature all-silicon micro-sensor based on the thermo-optic effect," IEEE Trans. Electron Devices **44**, 766–774 (1997).
12. G. Cocorullo, F. G. Della Corte, and I. Rendina, "Temperature dependence of the thermo-optic coefficient in crystalline silicon between room temperature and 550 K at the wavelength of 1523 nm," Appl. Phys. Lett. **74**, 3338–3340 (1999).
13. J. Komma, C. Schwarz, G. Hofmann, *et al.*, "Thermo-optic coefficient of silicon at 1550 nm and cryogenic temperatures," Appl. Phys. Lett. **101**, 041905 (2012).
14. B. J. Frey, D. B. Leviton, and T. J. Madison, "Temperature-dependent refractive index of silicon and germanium," Proc. SPIE **6273**, 62732J (2006).
15. M. A. Green and M. J. Keevers, "Optical properties of intrinsic silicon at 300 K," Prog. Photovolt. Res. Appl. **3**, 189–192 (1995).
16. A. Karoui and A. Kechiantz, "Quantum Mechanics design of two photon processes based solar cells," in *Some Applications of Quantum Mechanics*, M. R. Pahlavani, ed. (InTech, 2012).
17. M. Born and E. Wolf, *Principles of Optics: Electromagnetic Theory of Propagation, Interference and Diffraction of Light*, 7th ed. (Cambridge University Press, 1999).
18. S. M. Kay, *Fundamentals of statistical signal processing: Estimation theory* (Prentice Hall, 1993).